Article

Thermal Characterization Study of Double End Face Grinding Powder Metallurgy Stainless Steel 316L

Yue Lu [1], Junchao Feng [2], Cong Sun [1,*], Kaiyuan Lin [1], Guanlong Wang [1] and Xin Wang [1]

[1] School of Mechanical Engineering and Automation, Northeastern University, Shenyang 110819, China;
     yuelu_neu@163.com (Y.L.); 13734863846@163.com (K.L.); 583744842@qq.com (G.W.); wx1046985474@163.com (X.W.)
[2] School of Mechanical and Power Engineering, Dalian Ocean University, Dalian 116023, China; a1200474@126.com (J.F.)

* Corresponding author. E-mail: suncong1@mail.neu.edu.cn (C.S.)

ABSTRACT: Double end face grinding machining is a highly efficient surface grinding technique. And grinding temperature is an important factor affecting the surface quality of workpieces. However, it is difficult to monitor the surface temperature of the workpiece in real time because of the covered contact between the grinding wheel and the upper and lower surfaces of the workpiece during the machining process. This paper aims to conduct a mechanistic analysis and experimental investigation of the machining process to address this challenge. Initially, the paper conducts an analysis of the kinematic mechanism, modal analysis, and the grinding force mechanism specific to the double end face grinding process. Afterwards, the mechanisms leading to the generation of grinding heat and the associated heat transfer mechanisms are explored in depth. The paper then proceeds to solve the instantaneous temperature field during double end face grinding by the finite element method (FEM). Furthermore, the micro and macro profile heights of the machined workpiece surfaces are measured and analyzed. The results show that the machined workpiece surface shows a high center and low edge. This is due to the fact that the temperature at the edge of the workpiece is higher than the center during machining, resulting in more material removal. Through these investigations, the study is able to determine the optimal process parameters for the machining process. This in turn improves machining efficiency and product conformity. And these findings not only guide practical production processes but also provide a foundation for future theoretical research in this area.

Keywords: Double end face grinding; Modal analysis; Grinding force; Temperature field

1. Introduction

Grinding is a crucial machining process in the field of manufacturing, significantly affecting the surface quality of the machined components [1]. Double end face grinding is a type of face-contact grinding process, widely utilized in industry for its high machining efficiency [2]. However, studying the double end grinding mechanism is essential due to the process occurring in an enclosed environment, precluding real-time observation.

A substantial body of research has been dedicated to the theoretical modeling and experimental study of conventional grinding forces. Jamshidi et al. [3] developed a force model to predict average grinding force for Inconel 718 with electroplated CBN. Two methods, namely mechanistic and oblique cutting approaches, were employed and results were compared with the experiments. Results showed that grinding with CBN wheel led to lower force and force coefficients. Chang et al. [4] took into account the randomness of the abrasive grain distribution and proposed a closed form expression for the random grinding force as a function of the grinding conditions and the abrasive grain distribution. The results show that predictions drawn from the theoretical model are substantiated by the power spectrum density (PSD), variance, and time domain signal of the experimentally measured grinding forces under various grinding conditions. Li et al. [5] proposed an improved grinding force model by considering the abrasive grain geometry factor. And the experiments of dry grinding Ti-6Al-4V are designed. The experimental findings show that the values of numerical calculation and experimental measurement are in good agreement under different machining parameters, and the minimum error value is only 2.1%. Sun et al. [6] proposed a predictive model of grinding force in the silicon wafer self-rotating grinding process. In their article, the theoretical model includes cutting and sliding. Lastly, an optimized

two-step process is proposed to control subsurface cracks and simultaneously improve material removal rate according to the predictive model of grinding force. Shi et al. [7] conducted experimental studies to validate the impact of wheel speed on the distribution of normal force and subsequently refined the grinding force model. Tang et al. [8] optimized the grinding force model by considering factors such as grinding wheel speed, workpiece feed rate, and grinding depth and verified the results of the model calculation through experiments. Yang et al. [9] developed a grinding force prediction model based on analysis of scratch test and kinematics of ultrasonic vibration assisted grinding (UVAG), and the validity of the model is verified by the experiment designed. It can be found that the grinding force is decreased with the increase of spindle speed (n) and amplitude (A(a)). Lei et al. [10] established a new dynamic grinding force model for ultrasound-assisted single-grain high-speed grinding in order to explore the effect of ultrasound-assisted grinding on the grinding force during the machining process, based on the fact that the abrasive grits are constantly worn out during the grinding process. Cai et al. [11] proposed a dynamic grinding force model based on the grain element method in order to predict the peripheral grinding force during the grinding process. The model divides a grain into multiple grain elements and assumes that each element has a rectangular cross-section. In Ding's study [12], an iterative blending integrating a grinding force model that comprehensively considers the impact of grain size and dislocation density evolution of the material is proposed. The results indicate that the implementation of an iterative blending scheme is instrumental in obtaining a more accurate prediction of the grinding force and a deeper insight of the influence mechanisms of materials microstructure on the grinding process. Ma et al. [13] established a grinding force predictive model for the LAG process, which has taken the combined effects of temperature-dependent mechanical properties of the material, statuses of grit-material micro interaction, and stochastic shapes and random distributions of abrasive grits into consideration. And it is demonstrated that the grinding force can be reduced by a certain percentage ranging from 29.4–60.1% using the optimal machining parameters. Li et al. [14] provide a comprehensive analysis of material removal behavior and a review of grinding force models, providing scientists with a variety of valuable insights into material removal mechanisms and modeling of grinding forces. Accordingly, Meng et al. [15] also provided a detailed review of grinding force modeling methods. The aforementioned research holds significant guiding significance for establishing a model of grinding forces in double-sided grinding.

The large amount of heat generated during the grinding process directly affects the workpiece and the grinding wheel [16–20]. When attaining a higher temperature, a phase change occurs in the surface layer of the workpiece, resulting in the grinding burns. Additionally, residual stresses and cracks may persist post-cooling [21]. Jiang et al. [22] proposed an integrated model that combines the microscopic grit-workpiece interaction mechanism with the grinding temperature field, and the experimental results are consistent with the simulation results, which improves the accuracy of the grinding force and grinding temperature prediction. Ding et al. [23] investigated the temperature field during the grinding process using fluted grinding wheels, proposed a triangular intermittent heat source simulation method that is more in line with the actual grinding situation, and explored the variable parameters of the grinding temperature of fluted grinding wheels. Wang et al. [24] proposed a grinding temperature field prediction model by meshless finite block method with double infinite element. The simulation and experimental results are in good agreement, while outperforming FEM (ABAQUS) in terms of convergence and accuracy. Chen et al. [25] proposed an improved finite difference method for three-dimensional grinding temperature fields. The difference equations of boundary nodes and internal nodes are unified by adding auxiliary nodes, and the temperature distribution characteristics of the grinding temperature field are analyzed. The computational efficiency is improved by about 20%. Wang et al. [26] employed the finite element method (FEM) to analyze the changing characteristics of sliding friction. They determined that the maximum action point of sliding friction contact is the rear end of the contact area. Zhang et al. [27] conducted a study in which they measured the temperature during high-speed/efficiency grinding of 45 structural steel and 40Cr alloy steel. They then validated their findings through FEM analysis. In their experimental study, Mao et al. [28] explored the dynamics of surface grinding temperature. They investigated the impact of grinding contact zone length and heat distribution on the temperature field during grinding. Additionally, they proposed a novel numerical simulation method for surface grinding temperature fields. Concurrently, they delved into the intricacies of grinding the white layer, emphasizing its multifaceted nature and the influence of factors. Jin et al. [29] conducted a three-dimensional FEM simulation of transient heat transfer under efficient deep grinding conditions to predict the maximum surface temperature of the workpiece. The simulation results were consistent with those of the two-dimensional model simulation and were corroborated by experiments. These findings suggest that the heat source model would not significantly impact the simulation outcomes. Wang et al. [30] employed the FEM to construct a mathematical model of the temperature field of wet grinding and solved the isothermal map. A comparison of the FEM with the analytical solution revealed that the former is characterized by enhanced accuracy, reduced computational demands, and a broader

application scope. Li et al. [31] investigated the grinding temperature of minimum quantity lubricant cooling (MQLC) for heat transfer. A numerical simulation heat transfer model conducting the finite difference method was established for the numerical analysis of the MQLC grinding temperature. Results indicated that the model predictions and experimental results are in good agreement, with a 4.8% average model error. The heat transfer mechanism of the nanofluids was also analyzed. For an in-depth understanding of profile grinding temperature distribution, simulation and experimental studies were conducted on the thermal analysis. Accordingly, Li et al. [32] simulated and predicted grinding temperature via the finite element model. The results showed simulation results can accurately describe the grinding temperature distribution of the slot structure, and the prediction error was approximately 17% to 18%. Lan et al. [33] used the temperature matching method to establish a heat source model for the contact zone in the actual grinding process based on the inverse heat source principle and the actual measured grinding temperature. The variation of the workpiece grinding temperature field was simulated using the finite element method. The results show that the heat source model established according to the temperature matching method is in good agreement with the measured values at different depths underground, with relative errors ranging from 1.8% to 8%. Hong et al. [34] proposed a temperature measurement method based on metallographic images and a cyclic feedback algorithm, which effectively solved the problem of accurate grinding temperature measurement due to the spatial limitation of the grinding contact area and the time variation of the heat source by reconstructing the grinding temperature field and innovatively applied the cyclic feedback algorithm of differential heat transfer to solve the problem of the dynamic temperature field distribution under a random heat source.

As the grinding heat is a critical factor affecting the surface quality of the workpiece, many scholars have conducted in-depth research on the form and mechanism of cooling in the grinding process. Zhang et al. [35] applied nanoparticles in the cooling lubrication of grinding and theoretically analyzed the impact of cooling lubrication on the grinding surface through the energy ratio coefficient and specific grinding energy. The results showed that the best cooling effects occurred under the 2% volume concentration of CNT nanoparticles. Jia et al. [36] found that nanofluid minimum quantity lubrication(NMQL) can improve grinding performance in terms of cooling and lubrication and is ecofriendly because it consumes a small amount of grinding fluid. Ultrasonic machining can improve grinding performance owing to its reciprocating vibration mechanism and furrow widening. Xu et al. [37] conducted a preliminary exploratory study on electrostatic atomization MQL. Previous experiments have shown that electrostatic atomization MQL can reduce tool wear by 42.4% in metal cutting and improve the machined surface R(a) by 47% compared with pneumatic atomization MQL. Gao et al. [38] found that the vegetable oil-based nanofluid minimum quantity lubrication (NMQL) involving CNTs with excellent heat transfer and friction reduction can eliminate defects and dust from the original process. Sieniawski et al. [39] presented an innovative system of zonal centrifugal grinding fluid provision into the grinding zone. This system enables a major reduction in grinding fluid flow rate by precisely supplying the fluid directly into the grinding wheel's and machined material's contact area. It has been proven that the application of the zonal centrifugal cooling method, combined with lubrication of the grinding zone, positively impacts the residual stresses in the workpiece's surface layer, despite the grinding fluid flow rate having been limited by 90%. Mandal et al. [40] developed a pneumatic barrier setup for the first time for restricting the stiff air layer around the grinding wheel. Using the pneumatic barrier, a reduction of air pressure up to 53% has been observed experimentally. Hence, it reduces wastage of grinding fluid, leading to few environmental problems. Mihic et al. [41] provided a set of research oriented computational fluid dynamics (CFD) 3D models used to simulate the fluid flow and heat transfer in a grinding process. The simulation results agree well with experimental global flow rates, temperature, and pressure values, showing the feasibility of CFD simulations in grinding applications. Majumdar et al. [42] used the scraper board in experiments to find the critical region where the air pressure is zero. The coolant jet has then impinged into the grinding zone, which is maintained within the critical region. The requirement of specific energy, surface texture, and mechanical properties of the ground surface are analyzed and compared with the traditional grinding and the grinding at various positions of the scraper board.

The flow field for end face grinding has also been analyzed accordingly by some scholar. Zhang [43] analyzed the efficiency of the coolant flow field in the double-face grinding contact area. According to the typical structure of the double-face grinding wheel, the flow analysis of the groove grinding wheel with different shapes was simulated and analyzed. The research shows that slotting the grinding wheel can improve the effective flow and flow rate, and the cooling effect of the straight groove and 30° chute is better. Zou et al. [44] studied the effects of grinding wheel speed and workpiece speed on the coolant distribution law. The unidirectional flow field model in double-face grinding is established based on the contact equation of computational fluid dynamics, the Navier–Stokes equation, and the turbulence equation. The results show that the component surface fluid velocity gradually rises from the inner to the outside diameter of the grinding wheel.

In summary, the study on FEM simulation and experiment of the temperature field of double end face grinding is not sufficiently exhaustive. Consequently, this paper employs FEM software to carry out temperature field simulation and relevant process tests. In this paper, firstly, the mechanism of motion, modal analysis, and grinding force mechanism of the double end face grinding process are analyzed. Subsequently, the generation of grinding heat and the heat transfer mechanism are investigated to simulate the temperature field of double end face grinding. Finally, the micro/macro profile height of the machined workpiece surface is measured to obtain the optimum machining process parameters.

2. The Mechanism Analysis of Double End Face Grinding

In general, the relative motion process between the grinding wheel and the workpiece during the double end face grinding process differs from that of the conventional grinding process. The velocity of any point on the surface of the workpiece and the grinding force are different due to the rotation of the workpiece and the grinding wheel. Consequently, it is imperative to theoretically analyze the mechanism of double end face grinding machining. Therefore, this section carries out a modal analysis of the grinding wheel/workpiece system during machining and then determines the corresponding process parameters to avoid the resonance phenomenon of the system. At the same time, the grinding force model of a single abrasive grain was constructed, and the distribution of abrasive grains in contact with the workpiece surface was analyzed.

2.1. The Principle of Double Face Grinding

As illustrated in Figure 1, the double end face grinding process entails the placement of the workpiece on the feeder plate, with the upper and lower grinding wheels driven by the spindle, respectively. During the processing phase, both the workpiece and the grinding wheel rotate concurrently, thereby facilitating the removal of surface material. The workpiece, a cylinder with a diameter of $\varphi40$ mm and a height of 10 mm, is composed of stainless steel 316L. The upper and lower grinding wheels are composed of cubic boron nitride (CBN), with an outer diameter of $\varphi305$ mm, a width of 42 mm, a particle size of 140/170, and a density of 4.4 g/cm^3.
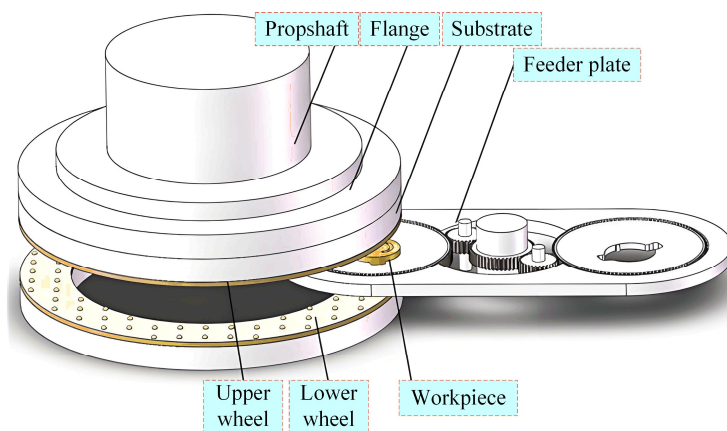

Figure 1. Double end face grinding process.

2.2. The Modal Analysis of Double Face Grinding Process

Modal analysis is a method used to determine the natural frequency of a system during vibration and the corresponding vibration mode. This information is essential for determining the required wheel speed for steady-state operation. The first twelve orders of the natural frequency and the corresponding modes of vibration are solved for the grinding wheel/workpiece system.

The material parameters necessary for the construction of the model are enumerated in Appendix Table A1 [45], and the solution process and results are demonstrated in Figure 2. The grinding wheel and the workpiece are modeled as a whole, and the Solid 5 element is selected to mesh the created model. The cloud diagrams of the first six orders of vibration modes obtained are shown in Figure 2c,d. and the corresponding frequency results obtained are shown in Figure 2i. The first-order natural frequency, which is the smallest at 268.16 Hz, corresponds to a rotational speed of 1608 r/min. To prevent resonance phenomena during the experimental process, it is essential to adjust the rotational speed of the grinding wheel appropriately.
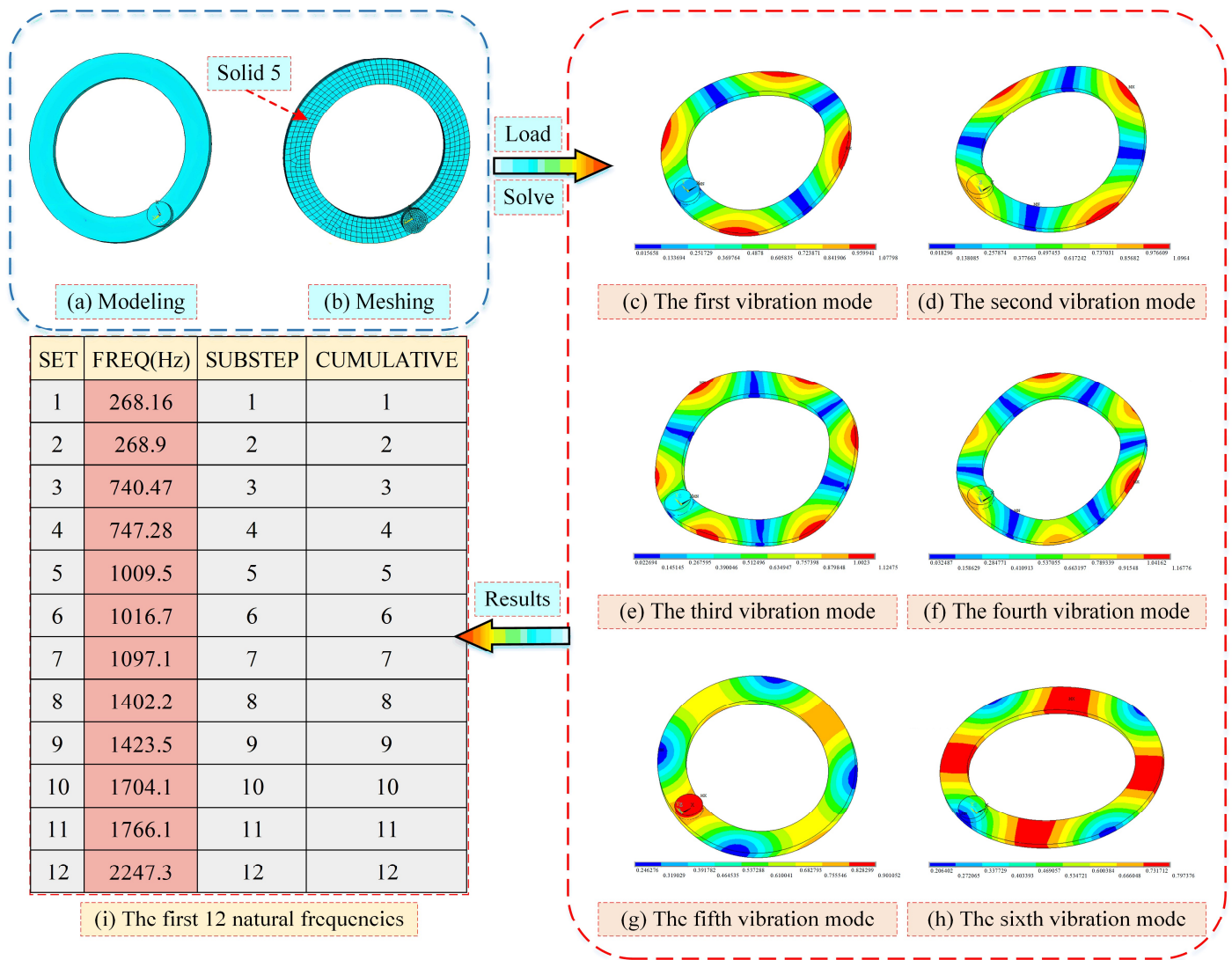
SET	FREQ(Hz)	SUBSTEP	CUMULATIVE
1	268.16	1	1
2	268.9	2	2
3	740.47	3	3
4	747.28	4	4
5	1009.5	5	5
6	1016.7	6	6
7	1097.1	7	7
8	1402.2	8	8
9	1423.5	9	9
10	1704.1	10	10
11	1766.1	11	11
12	2247.3	12	12

Figure 2. The modal analysis of double end face grinding process.

2.3. Calculation of Grinding Force during Machining

The geometry of the abrasive grain is random, and for the purposes of calculation, the grain is simplified to a sphere [46]. Figure 3b shows that not all the abrasive grains are involved in material removal during the process due to the different protrusion height of each abrasive grain. From the mechanism of formation, the grinding force can be categorized into normal force F_n and tangential force F_t [47], as shown in Figure 3c. The grinding forces consist of two components: friction force and chip force. And the following relationship is expressed by:

$$F_n = F_{ns} + F_{nc}$$
$$F_t = F_{ts} + F_{tc}$$

(1)

(a) planform

(b) sectional view
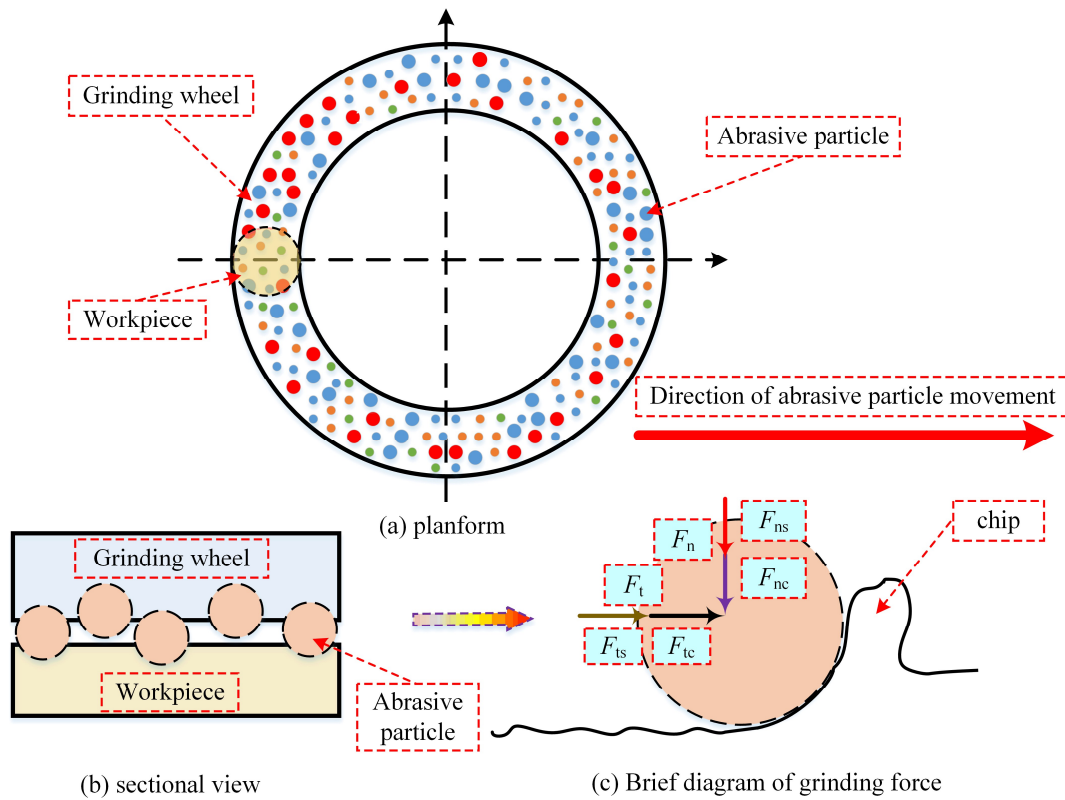
(c) Brief diagram of grinding force

Figure 3. Detailed illustration of the discretized grinding system: (**a**) planform of the detailed illustration, (**b**) sectional view for the interactions between the wheel and the workpiece, (**c**) diagram for the formation of the single abrasive grinding force.

2.3.1. The Calculation of the Grinding Force of a Single Abrasive Grain

During the machining process, the abrasive grains are in elastic contact with the workpiece, and based on the Hertzian elastic contact theory [48,49], the normal friction force F_{ns} can be expressed as [8]:

$$F_{ns} = \sqrt{\frac{16d_a^3 \cdot R_e \cdot E^{*2}}{9}} \tag{2}$$

where E^* is the equivalent modulus of elasticity, which is expressed as $1/E^* = (1 - v_1^2)/E_1 + (1 - v_2^2)/E_2$. v_1 and v_2 are the poisson's ratio of workpiece and CBN abrasive grains, respectively. E_1 and E_2 are the elastic modulus of the workpiece and CBN abrasive grains, respectively. Consequently, the tangential force friction F_{ts} can be expressed as:

$$F_{ts} = \mu F_{ns} \tag{3}$$

In order to establish a cutting force model, the cutting process of a single abrasive grain is equated to a single-point cut, where the material is removed continuously to form a chip with a fixed cross-sectional area [50]. For this purpose, the normal cutting force F_{nc} can be expressed as:

$$F_{nc} = k \cdot A \tag{4}$$

where k is the chip thickness coefficient related to the material properties and A is the abrasive cutting area.

The ratio of the tangential chip force F_{tc} to the normal force F_{nc} is constant during chip formation. Thus, the tangential chip force F_{tc} can be expressed as:

$$F_{tc} = \varphi F_{nc} \tag{5}$$

where φ is generally taken as 0.6 [51]. In conclusion, for a single abrasive grain, the normal and tangential grinding force can be expressed as:

$$F_n = F_{ns} + F_{nc} = \sqrt{\frac{16 d_a^3 \cdot R_e \cdot E^{*2}}{9}} + k \cdot A$$

$$F_t = F_{ts} + F_{tc} = \mu \sqrt{\frac{16 d_a^3 \cdot R_e \cdot E^{*2}}{9}} + \varphi k \cdot A$$

(6)

2.3.2. The Simulation of Grinding Wheel Morphology and Effective Contact Area

For the given grinding wheel [46], the maximum(d_{max}) and minimum(d_{min}) diameters of the grains can be determined. Based on these, the mean diameter(d_{mean}) of the abrasive grains can be derived as a function of $d_{mean} = (d_{max} + d_{min})/2$. The distribution of the grain dimensions for any given wheel usually takes the form of normal distribution. And the standard deviation is set as $\sigma = (d_{max} - d_{min})/4.4$. Hence, the probability density function of grain diameter can be express as:

$$f(x) = \frac{1}{\sqrt{2\pi}\sigma} \exp\left(-\frac{(d_{gx} - d_{mean})^2}{2\sigma^2}\right)$$

(7)

The maximum diameter d_{max} and the average diameter d_{mean} of the abrasive grains are equivalent to the maximum protruding height h_{max} and the average protruding height of the abrasive grains h_{mean} respectively [52]. The protruding height of the abrasive grain h_{gx} adheres to a normal distribution, with a standard deviation $\sigma = (h_{max} - h_{mean})/3$. Therefore, the probability density function of the protruding height of the abrasive grains can be expressed as follows:

$$P(x) = \frac{3}{\sqrt{2\pi}(h_{max} - h_{mean})} \exp\left(-\frac{1}{2}\left[\frac{3(h_{gx} - h_{mean})}{h_{max} - h_{mean}}\right]^2\right)$$

(8)

In this paper, the mesh number of the grinding wheel abrasive grains is 140/170, and the statistical results of the abrasive grain size on the grinding wheel are shown in Figure 4a. The effective contact area of the grinding wheel/workpiece is illustrated in Figure 4b, with the two planes A and B denoting the range of effective abrasive grains. In turn, the grinding depth of the grit can be determined.
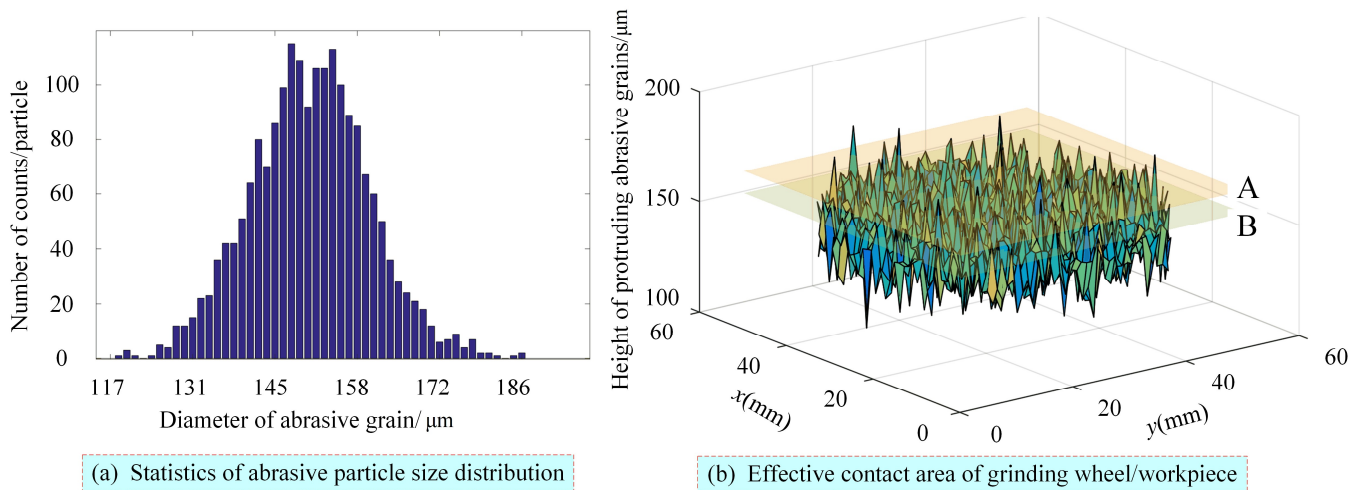

(a) Statistics of abrasive particle size distribution

(b) Effective contact area of grinding wheel/workpiece

Figure 4. Analysis of grinding wheel/workpiece contact.

In summary, in this section, a modal analysis of the grinding wheel/workpiece system during machining is first carried out, which can determine a reasonable grinding wheel rotation speed and thus avoid the resonance phenomenon of the system. At the same time, the constructed model of the grinding force of a single abrasive grain and the surface contact of the abrasive grain/workpiece can further clarify the machining process mechanism.

3. The Theoretical Study on Thermal Performance of Double End Face Grinding

During double end face grinding, the contact area between the grinding wheel and the workpiece surface is closed, resulting in low heat dissipation. Consequently, conducting a thermal analysis of the machining process is imperative.

In this section, the analysis process of the FEM method is firstly introduced, then the heat transfer fundamentals are analyzed, and finally the heat flow density loading equations of the FEM model are determined, which are used as parameter inputs for the temperature field solution in the next section.

3.1. The Study Methods of Thermal Performance

The grinding temperature is determined by material properties, grinding dosage, grinding wheel characteristics, and grinding fluid. When solving the grinding temperature field, the approximate analytical method based on the theory of moving heat sources or the numerical solution method dominated by discrete mathematics is generally used. Currently, the finite difference method (FDM), finite volume method (FVM), and FEM are the three most commonly used numerical solution methods. In this paper, the FEM is employed to solve the temperature field of the workpiece surface during the grinding process.

As illustrated in Figure 5, the FEM solution process of the grinding temperature field is as follows: Initially, the element type, material properties, and other parameters are specified in the preprocessor. Then, the model is established, and the meshing is completed.
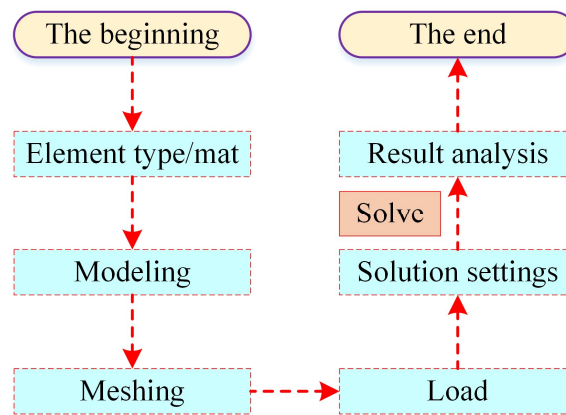

Figure 5. Flow chart of FEM analysis of temperature field.

3.2. Theoretical Foundation of Heat Transfer

The differential equation for heat transfer based on the law of conservation of energy is as follows:

$$-\left(\frac{\partial q_{\mathrm{x}}}{\partial x}+\frac{\partial q_{\mathrm{y}}}{\partial y}\right)+Q-c\frac{\partial T}{\partial t}=0 \tag{9}$$

where c represents the volumetric heat capacity, Q represents the rate of heat generation per unit volume inside the object, q represents the heat flux, t represents time. In addition, $-(\partial q_x/\partial x+\partial q_y/\partial y)$ represents the amount of heat conducted from the outside to the system per unit volume per unit time.

The schematic of the heat transfer principle for FEM calculations is presented in Figure 6. In this figure, each discrete calculation element corresponds to a specific heat flow density and instantaneous temperature. It is also important to note that the influence of thermal effects exists between neighboring calculation elements.
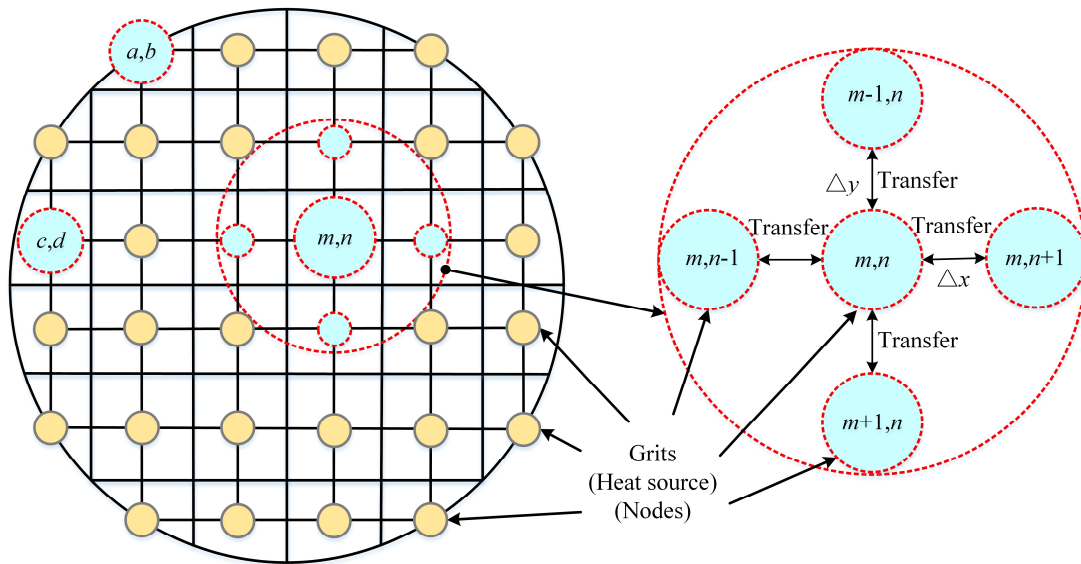
Figure 6. Illustration of the heat transfer principle.

3.3. Surface Heat Flux Analysis of the Grinding Process

In this paper, the distribution of heat flux density is simplified to a one-dimensional heat conduction problem, and only the z-direction heat flux transfer is considered. Wang employed the FEM to simulate and analyze the temperature of the grinding zone. A comparison of this calculation method's results with experimental data revealed an error margin of 12%. Consequently, the heat source load curve for the double end face grinding condition can be obtained as shown in Figure 7.
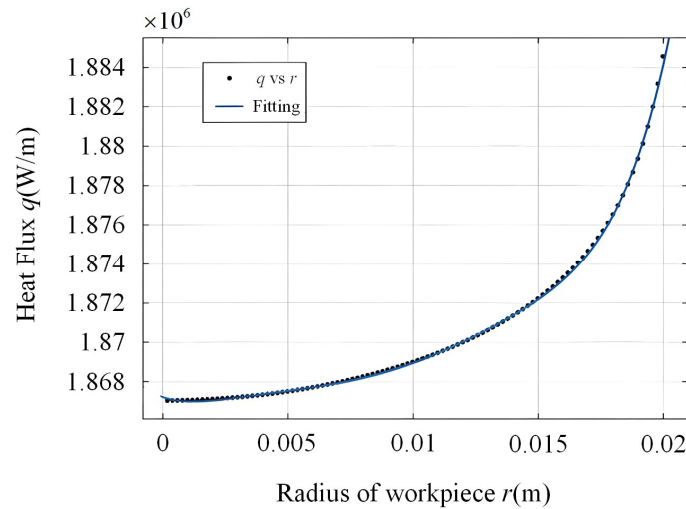

Figure 7. Fitting curve of heat source.

As a result, the expression for the heat source as a function of radius can be obtained as follows:

$$f(x) = p1 \times x^6 + p2 \times x^5 + p3 \times x^4 + p4 \times x^3 + p5 \times x^2 + p6 \times x + p7$$

$$\begin{cases} p1 = 5.955e+15 \\ p2 = -3.063e+14 \\ p3 = 6.05e+12 \\ p4 = -5.606e+10 \\ p5 = 2.631e+08 \\ p6 = -4.341e+05 \\ p7 = 1.867e+06 \end{cases}$$
(10)

In summary, this section clarifies the FEM calculation process, analyzes the heat transfer mechanism in detail, and solves the heat flow density loading equation. The next section starts to solve the grinding temperature field.

4. The Temperature Field Simulation for Double End Face Grinding

The grinding temperature is a pivotal factor influencing the surface quality of the workpiece. Consequently, it is imperative to simulate the grinding temperature field during the machining process. In this section, the FEM software ANSYS is utilized to simulate and analyze the temperature field of the double end face grinding process. The material parameters of the grinding wheel and the workpiece are enumerated in Appendix Table A1.

The sequence of operations involved in the calculation of the temperature field is illustrated in Figure 8. Initially, the geometry model of the workpiece is created. Subsequently, the mesh of the workpiece is generated. Subsequently, the model is subjected to the application of heat flux density and convective heat transfer load. Concurrently, the initial temperature of the workpiece and the ambient temperature are set to 25 °C. Finally, the solution is carried out. As shown in Figure 8d, the temperature distribution on the workpiece surface at moment 3s for different working conditions. It can be seen that the temperature at the edge of the workpiece is higher than that at the center, and the grinding temperature increases with the increase of wheel speed. This is due to the higher heat flux at the edge of the workpiece. Thereby, the temperature distribution difference (higher edge and lower center) may result in machining inconsistency, removing more material from the edge part.
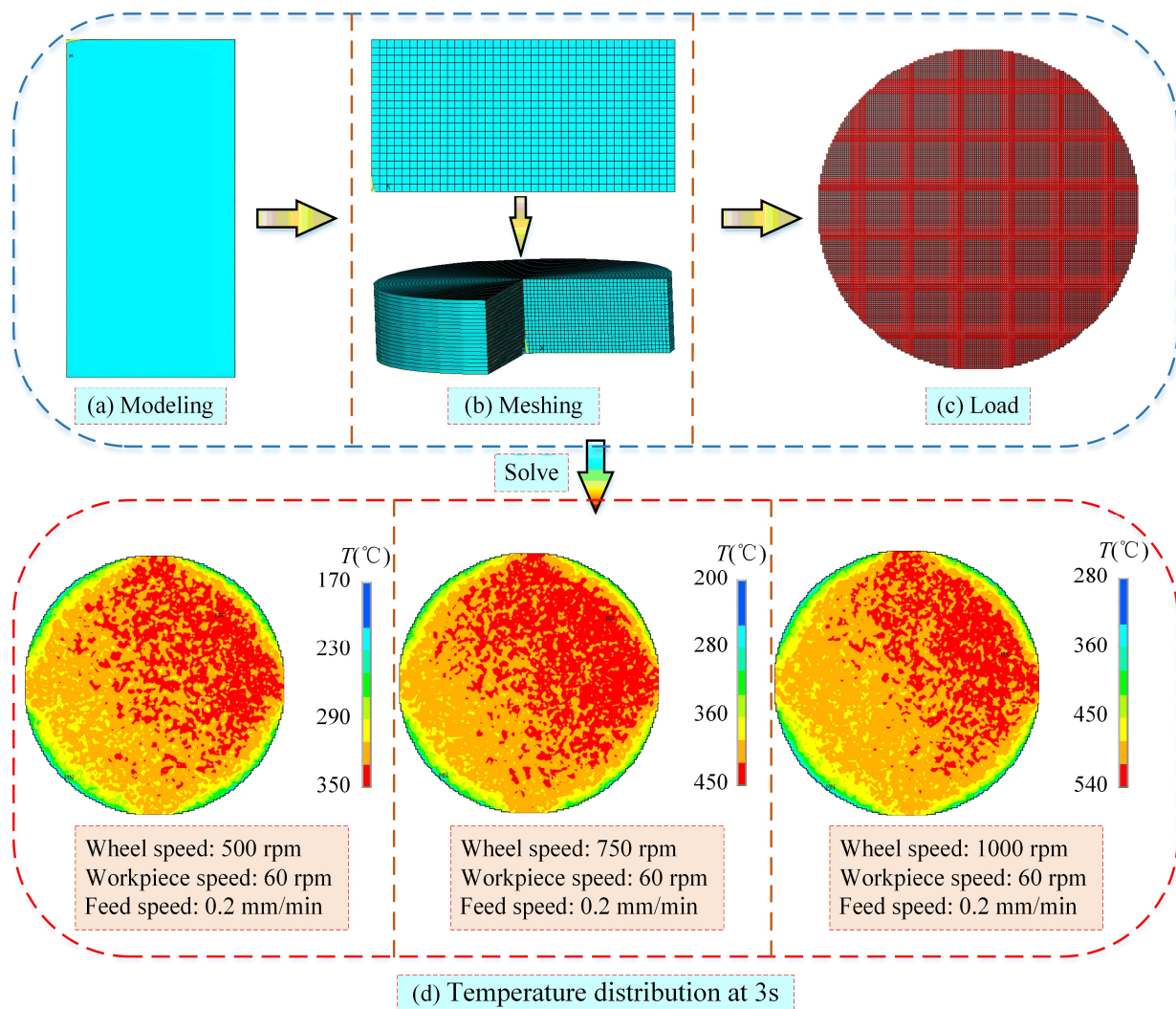

Figure 8. Calculation of FEM temperature field.

In summary, this section clarifies the distribution of the grinding temperature field on the surface of the workpiece, in order to verify the accuracy of the model. The verification is carried out by the height of the workpiece surface profile machined under different parameter combinations in the next section.

5. Experimental Study of Surface Removal Uniformity on Double End Face Grinding

In order to validate the temperature distribution characteristic on the machining effect, the related experiments are designed with multiple selective parameters. In the meantime, the microscopic contour morphology of the machined workpiece surface was observed, and the contour height of the machined workpiece surface was measured.

5.1. Parameters Related to Grinding Experiments

The experiment was conducted using the HMP-108 computerized CNC end grinding machine, as depicted in Figure 9. The technical parameters of the grinder are enumerated in Appendix Table A2.
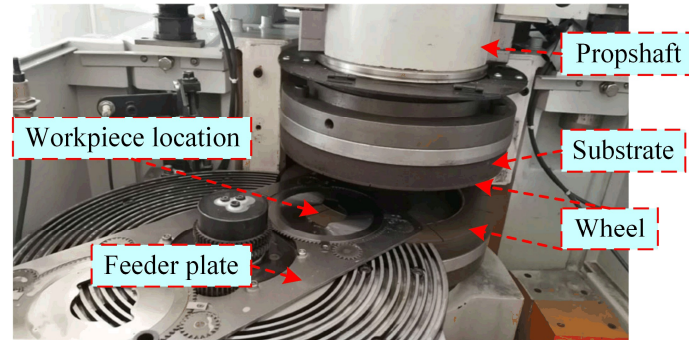

Figure 9. HMP-108 Computerized CNC face grinding machine.

The experimental parameters are shown in Table 1.

Table 1. Processing parameters of double end face grinding experiment.

Number	Feed Speed mm/min	Feed Distance mm	Working Condition	Wheel Speed r/min	Workpiece Speed r/min
A	0.2	0.05		1150	80
B	0.2	0.1		1150	80
C	0.4	0.05		1150	80
D	0.4	0.1	wet grinding	1150	80
E	0.6	0.05		1150	80
F	0.6	0.1		1150	80
G	0.8	0.05		1150	80
H	0.8	0.1		1150	80

5.2. Micro-Profile Height Measurement of Workpiece Surface

The surface morphology of the machined workpiece was observed by using a Leica DVM6 microscope, as shown in Figure 10.
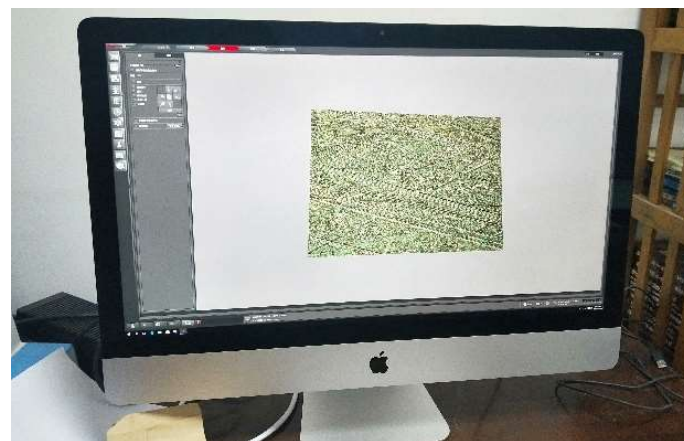

Figure 10. The Leica DVM6 microscope.

The workpiece conditions A–D are observed separately, and the results are shown in Figures 11–14. The center and edge positions of the workpiece are observed separately. It can be found that the trajectory at the center of the

workpiece is relatively sparse and the trajectory at the edge of the workpiece is relatively densely packed. This phenomenon can be attributed to the fact that positions away from the workpiece center exist in multiple spatial locations as the workpiece rotates. Consequently, the workpiece is exposed to a greater number of abrasive particles. Additionally, the standard deviation of the height of the workpiece surface line profile increases with the increase of the feed speed. At a feed speed of 0.2 mm/min, the standard deviation of the height of the workpiece surface line contour decreases with an increase in feed distance. Conversely, at a feed speed of 0.4 mm/min, an increase in feed distance is associated with a corresponding increase in the standard deviation.
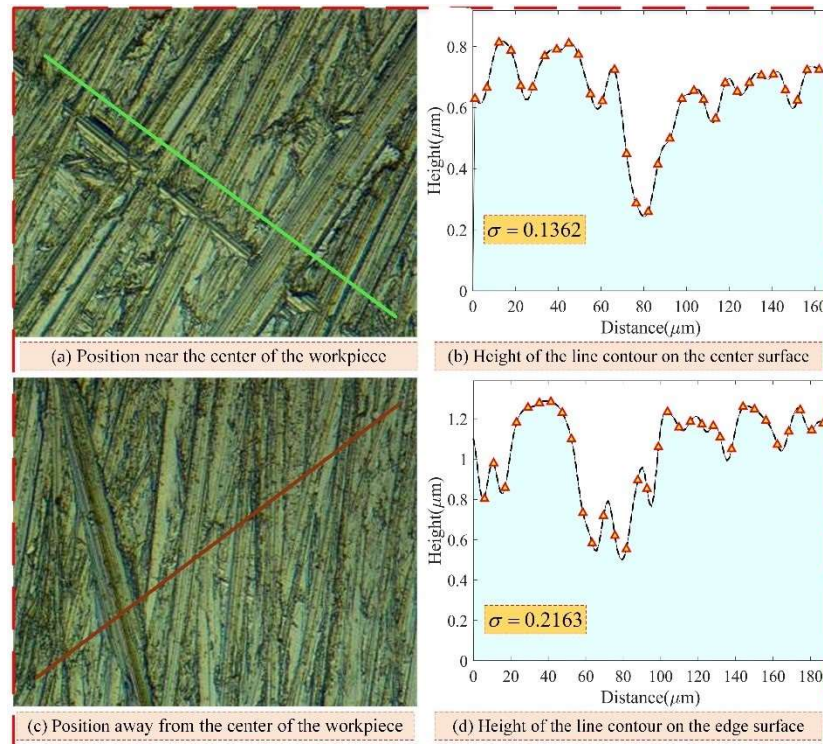

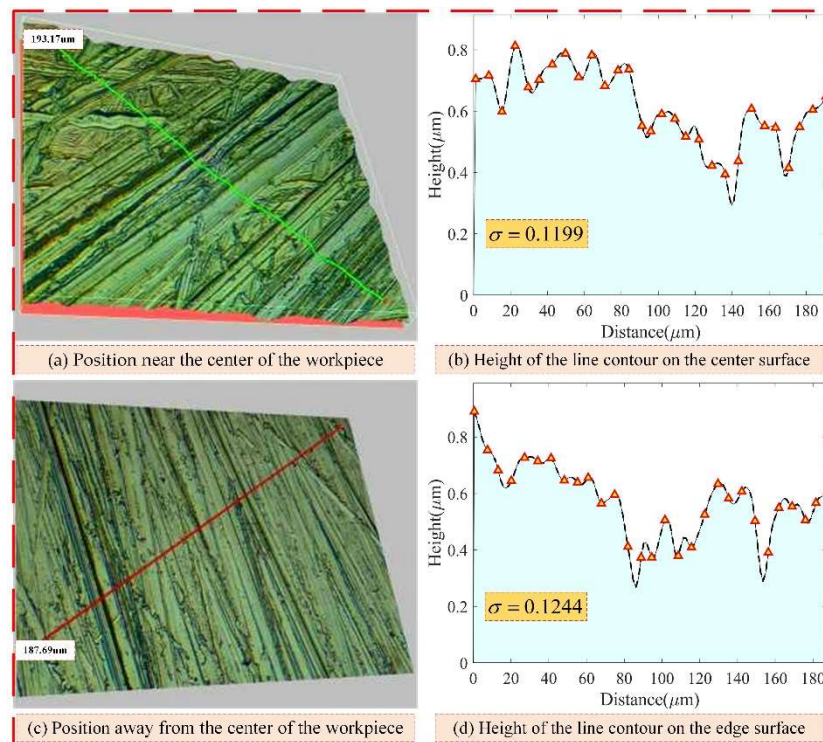**Figure 11.** The machined surface state of the condition A.
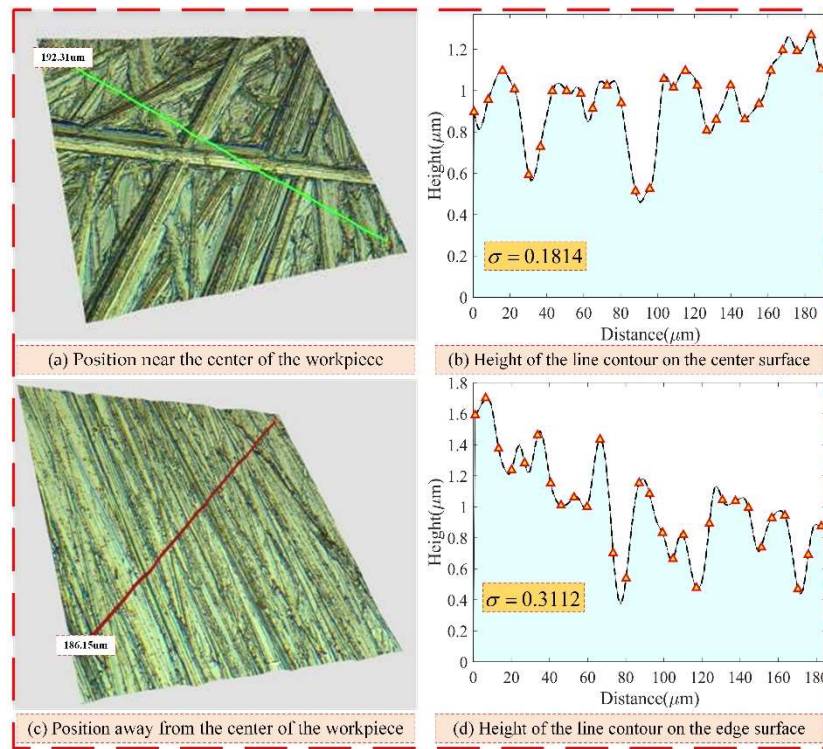

Figure 12. The machined surface state of the condition B.

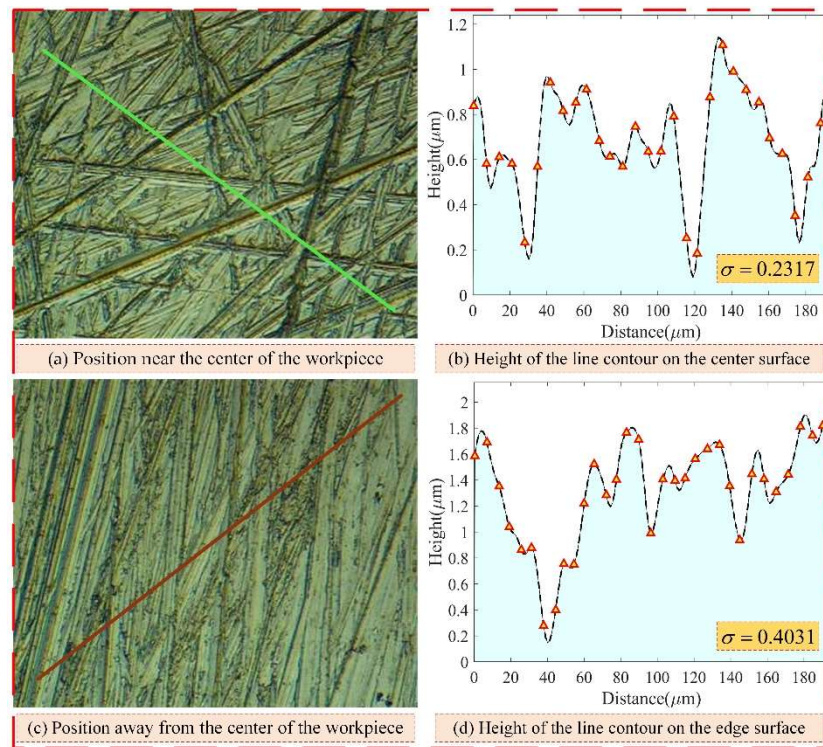**Figure 13.** The machined surface state of the condition C.

Figure 14. The machined surface state of the condition D.

5.3. Macro-Profile Height Measurement of Workpiece Surface

A dial indicator was utilized to ascertain the height of the profile on the workpiece surface, as illustrated in Figure 15a. To ensure the homogeneity of the measurement data, 10 points were selected at equal spacing in the four vertical directions (I represents the west, II represents the east, III represents the south and IV represents the north) on the workpiece surface for measurement. The average value of the measured values on the positions of the same radius was then taken, as shown in Figure 15b.
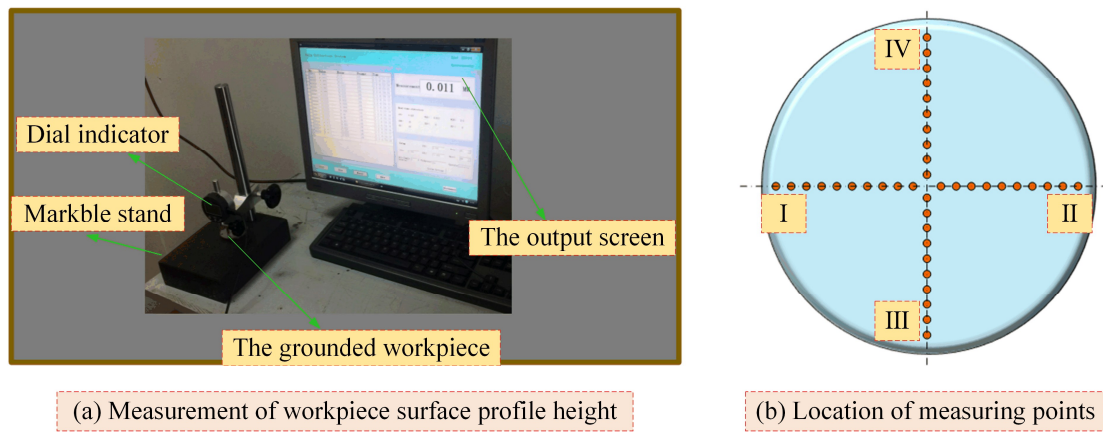
(a) Measurement of workpiece surface profile height   (b) Location of measuring points

Figure 15. Experimental data measurement.

The results of the measured data are shown in Figure 16. The results show that the surface of the machined workpiece shows a phenomenon of high center and low edge. This is due to the fact that more grinding heat is generated at the edge of the workpiece during the machining process, resulting in more material being removed at the edge.

From the figure, it can also be seen that when the feed speed is below 0.8 mm/min, the height difference of the surface profile of the workpiece decreases with the increase of the feed speed. At the same time, a smaller height difference can be obtained by increasing the feed distance. And when the feed speed is at 0.8 mm/min, the machining effect becomes bad. Therefore, the optimum process parameters for this study are as follows: The feed speed is 0.6 mm/min, the feed distance is 0.1 mm, the working condition is wet grinding, the speed of the grinding wheel is 1150 r/min, and the speed of the workpiece is 80 r/min.
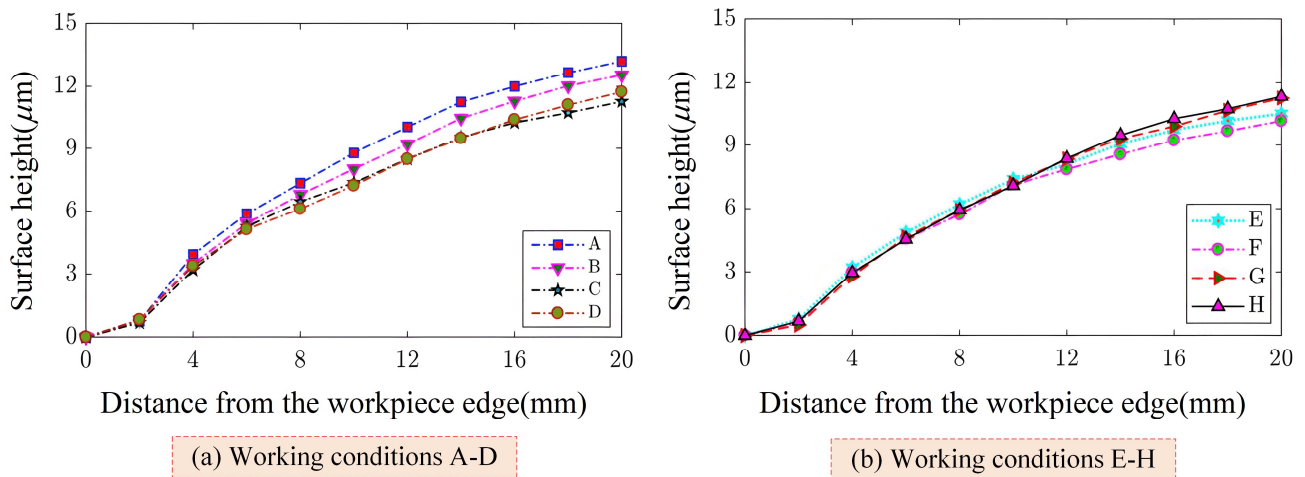

(a) Working conditions A-D   (b) Working conditions E-H

Figure 16. The measured height difference of the workpiece surface.

In this section, the microscopic contour morphology of the machined workpiece surface was observed, and the contour height of the machined workpiece surface was measured. It can be found that the simulation results are consistent with the trend of the surface profile characteristics of the experimental results. And the optimal process parameters were determined, which significantly improved the qualification rate and machining efficiency of the endface grinding process.

6. Conclusions

The double end face grinding process poses significant challenges in the detection of dynamic temperature information due to the closed configuration of both surfaces. This study proposes a methodology for simulating the grinding temperature field during the machining process, conducted by concurrent process experiments. The primary research conclusions of this study are as follows:

Modal analysis of the double end face grinding process was performed. The first-order natural frequency of the system is the smallest, which is 268.16 Hz, and the rotational speed corresponding to the natural frequency is 1608 r/min. In order to ensure the stability of the experimental process and to avoid resonance phenomena, an appropriate

grinding wheel speed is selected. Then the transient grinding temperature field on the workpiece surface was solved. It can be seen that the temperature at the edge of the workpiece is higher than that of the center part at moment 3s. This is due to the higher heat flux at the edge of the workpiece. Meanwhile, the grinding temperature increases as the wheel speed enhances. And the contour height difference of the machined workpiece surface was measured and analyzed. The surface of the machined workpiece shows a phenomenon of high center and low edge. This is due to the fact that more grinding heat is generated at the edge of the workpiece during the machining process, resulting in more material removed at the edge.

The optimal process parameters were determined by solving the grinding temperature field and experimental verification. And the optimized process significantly improves the machining efficiency and qualification rate. In this paper, a detailed mechanism analysis of the end face grinding process in confined form is carried out to provide some guiding reference for the machining of disk/chip parts.

Unfortunately, the convective heat transfer coefficients applied to the finite element model are loaded in the form of uniform loads in order to simplify the calculations in this paper. However, the distribution of the coolant flow field is extremely complex during actual processing, which can be studied in depth in subsequent work.

Appendix A

Table A1. Grinding wheel and workpiece material parameters.

Item	Thermal Conductivity (W/m·K)	Elastic Modulus (GPa)	Density (kg/m^3)	Poisson's Ratio	Specific Heat (J/kg·K)	Coefficient of Linear Expansion (1/K)	Friction Coefficien
CBN Wheel	383	680	7800	0.3	506	7×10^{-6}	0.3–0.4
316L	16.2	150	7200	0.4	520	1.73×10^{-5}	

Table A2. Technical parameters of grinding machine.

Item	Parameters
Workpiece diameter (mm)	Φ40
Workpiece height (mm)	2–50
Grinding wheel diameter (mm)	305
Grinding wheel feed speed (mm/min)	0.18–187.5
Processing time (s)	10–20
Grinding wheel motor power (kW)	11
Total machine power (kW)	18

Author Contributions

Conceptualization, C.S.; Methodology, C.S. and Y.L.; Software, Y.L.; Validation, J.F. and K.L.; Formal Analysis, G.W.; Investigation, X.W.; Resources, C.S.; Data Curation, J.F.; Writing—Original Draft Preparation, Y.L.; Writing—Review & Editing, C.S.; Visualization, Y.L.; Supervision, C.S.; Project Administration, C.S.; Funding Acquisition, C.S.

Ethics Statement

Not applicable.

Informed Consent Statement

Informed consent was obtained from all subjects involved in the study.

Data Availability Statement

No data was used for the research described in the article.

Funding

Declaration of Competing Interest

The authors declare that they have no known competing financial interests or personal relationships that could have appeared to influence the work reported in this paper.

References

1. Sun C, Xiu S, Hong Y, Kong X, Lu Y. Prediction on residual stress with mechanical-thermal and transformation coupled in DGH. *Int. J. Mech.Sci.* **2020**, *179*, 105629.
2. Sun C, Xiu S, Li Q, Wang J, Zhao Y. Research on the embossment phenomenon of disc grinding by workpiece's removal rate. *Arch. Civ. Mech. Eng.* **2019**, *19*, 739–755.
3. Jamshidi H, Yastıkcı B, Gürtan M, Budak E. Grinding force model for inconel 718 with CBN and conventional wheels. In Proceedings of the 6th International Conference on Virtual Machining Process Technology (VMPT), Montréal, QC, Canada, 29th May 2017–2nd June, 2017.
4. Chang H-C, Wang J-JJ. A stochastic grinding force model considering random grit distribution. *Int. J. Mach. Tools Manuf.* **2008**, *48*, 1335–1344.
5. Liu M, Li C, Zhang Y, Yang M, Gao T, Cui X, et al. Analysis of grinding mechanics and improved grinding force model based on randomized grain geometric characteristics. *Chin. J. Aeronaut.* **2023**, *36*, 160–193.
6. Sun J, Qin F, Chen P, An T. A predictive model of grinding force in silicon wafer self-rotating grinding. *Int. J. Mach. Tools Manuf.* **2016**, *109*, 74–86.
7. Shi Z, Attia H, Srinivasaraghavan M. Experimental investigations of the force distributions in the grinding contact zone. *Mach. Sci. Technol.* **2009**, *13*, 372–384.
8. Tang J, Du J, Chen Y. Modeling and experimental study of grinding forces in surface grinding. *J. Mater. Process. Tech.* **2009**, *209*, 2847–2854.
9. Yang Z, Zhu L, Lin B, Zhang G, Ni C, Sui T. The grinding force modeling and experimental study of ZrO_2 ceramic materials in ultrasonic vibration assisted grinding. *Ceram. Int.* **2019**, *45*, 8873–8889.
10. Lei X, Xiang D, Peng P, Liu G, Li B, Zhao B, et al. Establishment of dynamic grinding force model for ultrasonic-assisted single abrasive high-speed grinding. *J. Mater. Process. Technol.* **2022**, *300*, 117420.
11. Cai S, Yao B, Zheng Q, Cai Z, Feng W, Chen B, et al. Dynamic grinding force model for carbide insert peripheral grinding based on grain element method. *J. Manuf. Process.* **2020**, *58*, 1200–1210.
12. Ding Z, Zhao Y, Guo M, Guo W, Wu C, Liang S. An iterative blending integrating grinding force model considering grain size and dislocation density evolution. *Adv. Manuf.* **2023**, *11*, 428–443.
13. Ma Z, Wang Q, Chen H, Chen L, Qu S, Wang Z, et al. A grinding force predictive model and experimental validation for the laser-assisted grinding (LAG) process of zirconia ceramic. *J. Mater. Process. Technol.* **2022**, *302*, 117492.
14. Li L, Zhang Y, Cui X, Said Z, Sharma S, Liu M, et al. Mechanical behavior and modeling of grinding force: a comparative analysis. *J. Manuf. Process.* **2023**, *102*, 921–954.
15. Meng Q, Guo B, Zhao Q, Li H, Jackson M, Linke B, et al. Modelling of grinding mechanics: A review. *Chin. J. Aeronaut.* **2023**, *36*, 25–39.
16. Jamshidi H, Budak E. Grinding temperature modeling based on a time dependent heat source. *Procedia CIRP* **2018**, *77*, 299–302.
17. Gu B, Wang Y, Tan R, Zhang W. Research on the calculation method of grinding temperature field of spiral bevel gear based on generative machining. *J. Phys. Conf. Ser.* **2024**, *2761*, 012009.
18. Li C, Li J, Wang S, Zhang Q. Modeling and numerical simulation of the grinding temperature field with nanoparticle jet of MQL. *Adv. Mech. Eng.* **2013**, *5*, 5986984. doi:10.1155/2013/986984.
19. Ren J, Zhao L, Wang Y, Zhang C, Tian X. Finite element analysis of grinding temperature field with water vapor as coolants. *Adv. Mater. Res.* **2012**, *472–475*, 456–461.
20. Yang M, Kong M, Li C, Long Y, Zhang Y, Sharma S, et al. Temperature field model in surface grinding: A comparative assessment. *Int. J. Extrem. Manuf.* **2023**, *5*, 042011.
21. Wei C, Xu K, Li R, Hu D. Temperature modeling in end grinding of coated workpieces. *J. Shanghai Jiaotong Univ. (Sci.)* **2010**, *15*, 319–322.
22. Jiang J, Ge P, Sun S, Wang D, Wang Y, Yang Y. From the microscopic interaction mechanism to the grinding temperature field: an integrated modelling on the grinding process. *Int. J. Mach. Tools Manuf.* **2016**, *110*, 27–42.
23. Ding N, Li A, Cui S, Zhang J, Zhao H. Simulation research on grinding temperature field of grooved grinding wheel. In Proceedings of the 2022 IEEE 6th Information Technology and Mechatronics Engineering Conference (ITOEC), Chongqing, China 4–6 March 2022; Volume 6, pp. 1314–1318.

24. Wang Z, Yu T, Wang X, Zhang T, Zhao J, Wen P. Grinding temperature field prediction by meshless finite block method with double infinite element. *Int. J. Mech. Sci.* **2019**, *153*, 131–142.

25. Chen H, Zhao J, Dai Y, Wang Z, Yu T. Simulation of 3D grinding temperature field by using an improved finite difference method. *Int. J. Adv. Manuf. Technol.* **2020**, *108*, 3871–3884.

26. Wang B, Dong G, Xie Y. Numerical analysis of rolling—sliding contact with frictional heating. *China Mech. Eng.* **2002**, *13*, 1880–1883.

27. Zhang G. *The Researching of Ultra High Speed Grinding Temperature*; Hunan University: Changsha, China, 2006.

28. Mao C. *The Research on the Temperature Field and Thermal Damage in the Surface Grinding*; Hunan University: Changsha, China, 2006.

29. Jin T, Stephenson D J. Three dimensional finite element simulation of transient heat transfer in high efficiency deep grinding. *CIRPAnn.—Manuf. Technol.* **2004**, *53*, 259–262.

30. Wang L, Ge P, Qin Y, Liu, Zhen C, Sun J, et al. Analysis of wet-grinding temperature field based on finite element method. *J. Mech. Eng.* **2002**, *38*, 155–158.

31. Li B, Li C, Zhang Y, Wang Y, Yang M, Jia D, et al. Numerical and experimental research on the grinding temperature of minimum quantity lubrication cooling of different workpiece materials using vegetable oil-based nanofluids. *Int. J. Adv. Manuf. Technol.* **2017**, *93*, 1971–1988.

32. Li B, Ding W, Zhu Y, Li C, Ma X, Yang M, et al. Thermal analysis on profile grinding of turbine disc slots of powder metallurgy superalloy FGH96. *Int. Commun. Heat Mass Transf.* **2024**, *159*, 108207.

33. Lan S, Jiao F. Modeling of heat source in grinding zone and numerical simulation for grinding temperature field. *Int. J. Adv. Manuf. Technol.* **2019**, *103*, 3077–3086.

34. Hong Y, Xiu S, Sun C, Zhao Y, Zhang X. Metallographic method for temperature measurement: Reconstruction of grinding temperature field based on critical austenitizing depth and cyclic feedback algorithm. *J. Mater. Process. Technol.* **2022**, *310*, 117770.

35. Zhang D, Li C, Zhang Y, Jia D, Zhang X. Experimental research on the energy ratio coefficient and specific grinding energy in nanoparticle jet MQL grinding. *Int. J. Adv. Manuf. Technol.* **2015**, *78*, 1275–1288.

36. Jia D, Li C, Zhang Y, Yang M, Zhang X, Li R, et al. Experimental evaluation of surface topographies of nmql grinding zro2 ceramics combining multiangle ultrasonic vibration. *Int. J. Adv. Manuf. Technol.* **2018**, *100*, 457–473.

37. Xu W, Li C, Zhang Y, Ali H, Sharma S, Li R, et al. Electrostatic atomization minimum quantity lubrication machining: from mechanism to application. *Int. J. Extrem. Manuf.* **2022**, *4*, 042003.

38. Gao T, Li C, Jia D, Zhang Y, Yang M, Wang X, et al. Surface morphology assessment of cfrp transverse grinding using cnt nanofluid minimum quantity lubrication. *J. Clean. Prod.* **2020**, *277*, 123328.

39. Sieniawski J, Nadolny K. The effect upon grinding fluid demand and workpiece quality when an innovative zonal centrifugal provision method is implemented in the surface grinding of steel crv12. *J. Clean. Prod.* **2016**, *113*, 960–972.

40. Mandal B, Singh R, Das S, Banerjee S. Development of a grinding fluid delivery technique and its performance evaluation. *Mater. Manuf. Process.* **2012**, *27*, 436–442.

41. Mihic SD, Cioc S, Marinescu ID, Weismiller MC. Detailed study of fluid flow and heat transfer in the abrasive grinding contact using computational fluid dynamics methods. *J. Manuf. Sci. Eng. Trans. Asme* **2013**, *135*, 041002.

42. Majumdar S, Kumar S, Roy D, Chakraborty S, Das S. Improvement of lubrication and cooling in grinding. *Mater. Manuf. Process.* **2018**, *33*, 1459–1465.

43. Zhang G. *Efficiency Analysis of Coolant Flow Field in Double-Face Grinding Contact Area*; Northeastern University: Shen yang, China, 2020.

44. Zou X, Zhang G, Li Q, Xiu S, Kong X, Yao Y. Flow field analysis of grinding fluid in double-face grinding. *Int. J. Adv. Manuf. Technol.* **2024**, *131*, 2071–2085.

45. Sun C, Lu Y, Xiu S, Li Q, Zhang P. Analysis on the removal mechanism of disc grinding based on dynamic thermal–mechanical coupling. *Int. J. Mech. Mater. Des.* **2021**, *17*, 831–853.

46. Wang D, Ge P, Bi W, Jiang J. Grain trajectory and grain workpiece contact analyses for modeling of grinding force and energy partition. *Int. J. Adv. Manuf. Technol.* **2014**, *70*, 2111–2123.

47. Singh GK, Yadava V, Kumar R. Modelling and optimisation of electro-discharge diamond face grinding of cemented carbide–cobalt composite. *Int. J. Ind. Syst. Eng.* **2012**, *12*, 141–164.

48. Yip FC, Venart JES. An elastic analysis of the deformation of rough spheres, rough cylinders and rough annuli in contact. *J. Phys. D Appl. Phys.* **2002**, *4*, 1470.

49. Fu Q, Wu L, Wang H. A correction method for the tangential grinding force on high-speed rail grinding test—bed. *Eng. Mech.* **2016**, *33*, 205–210.

50. Liu S, Chen T, Wu C. Rotary ultrasonic face grinding of carbon fiber reinforced plastic (CFRP): A study on cutting force model. *Int. J. Adv. Manuf. Technol.* **2016**, *89*, 1–10.

51. Gatzen HH, Beck M. Investigations on the friction force anisotropy of the silicon lattice. *Wear* **2003**, *254*, 1122–1126.

52. Zhou X, Xi F. Modeling and predicting surface roughness of the grinding process. *Int. J. Mach. Tools Manuf.* **2002**, *42*, 969–977.